

Supplementary Information

High thermoelectric performance of environmentally friendly sodium-doped $\text{Cu}_2\text{ZnSnS}_4$ single crystal: Evidence of valleytronics based strategy.

Akira Nagaoka,^{*a} Kenji Yoshino,^b Taizo Masuda,^c Taylor D. Sparks,^d Michael A. Scarpulla^d and Kensuke Nishioka^a

^aResearch Center for Sustainable Energy & Environmental Engineering, University of Miyazaki, Miyazaki 889-2192, Japan

^bDepartment of Applied Physics and Electronic Engineering, University of Miyazaki, Miyazaki 889-2192, Japan

^cS-Frontier Division, Toyota Motor Corporation, Shizuoka 411-0019, Japan

^dDepartment of Materials Science and Engineering, University of Utah, Salt Lake City, Utah 84112 USA

*Corresponding author: nagaoka.akira.m0@cc.miyazaki-u.ac.jp

1. Single crystal growth

Traveling Heater Method (THM): It is generally difficult to grow high-quality $\text{Cu}_2\text{ZnSnS}_4$ (CZTS) single crystals from melt because this material grows through a peritectic reaction (liquid phase + ZnS solid phase) [S1]. On the other hand, growth by the THM based on solution growth, which can proceed below the melting point, is well-suited for high-quality CZTS single crystals.

Feed polycrystallines of CZTS were synthesized by using a melting reaction. Cu (99.999%), Zn (99.9999%), Sn (99.9999%), and S (99.999%) shots and Na_2S (99%) powder were used as starting materials. Prior to growth, Cu, Zn, and Sn were chemically etched with HCl solution for 60 s and then rinsed in ultrapure 18M Ω m water. The ingots (15 g) with nominal compositions were synthesized by mixing the described amounts of elements in a carbon-coated 2 mm wall thickness quartz ampoule with 9 mm inner diameter under high vacuum of 10^{-6} Torr and then flame-sealed off. In a vertical furnace, the sealed ampoule was heated at 200 °C/h to 650 °C and held at this temperature for 24 h to react the constituents and prevent explosion from the S overpressure. Then the sealed ampoule was heated at 80 °C/h to 1100 °C and held at this temperature for 24 h to complete the reaction and ensure homogenization. The ampoule was then removed from the furnace and allowed to cool rapidly in air.

The feed polycrystalline CZTS ingot (80 mol%) and Sn solvent (20 mol%) were loaded into a carbon-coated quartz ampoule 2 mm wall thickness quartz ampoule with 10 mm inner diameter. The ampoule was flame-sealed off under high vacuum of 10^{-6} Torr, and then inserted into the THM furnace. The THM furnace has three coil heaters (upper, main, and bottom) for controlling temperature gradient. The upper heater temperature of 800 °C was used to prevent a sulfur deficiency in the grown CZTS crystal. The sulfur species evaporated from liquid zone

condensed on the cold wall of the ampoule without heating the upper part, thereby reducing the sulfur mole fraction in the crystal. For the THM growth, the main heater temperature (growth temperature) was 850 °C which is 50 °C higher than liquids temperature, and temperature gradient between the main and bottom heaters (the supersaturation region for single crystal growth) was about 40 °C/cm. This temperature gradient can control the length of solution zone 1 cm. The growth speed was 4-5 mm/day for 10 days. The dimensions of single crystal ingot are 10 mm in diameter and 40 mm length including zone solution region.

2. Characterization

Structural properties

The combination of X-ray diffraction (XRD) and Raman spectroscopy is a useful tool for investigation of secondary phases because the XRD peaks of CZTS overlap well with those of Cu_2S and ZnS , especially. The result details of both measurements are reported in our previous papers [S2-3]. The powder XRD pattern of each composition of samples exhibits major peaks corresponding to diffraction lines of the kesterite structure of CZTS (ICDD data #01-075-4122) in Supplementary Fig. 1a. The distinct peak at around $2\theta = 18.3$ can be observed for distinguishing between the kesterite and stannite structures. Samples in this study have the kesterite structure without secondary phases from XRD measurement. No secondary phases, such as Cu_2SnS_3 and ZnS , were observed in Raman measurement, as shown in Supplementary Fig. 1b. The spectra show clearly the CZTS peaks at 287, 337, and 371 cm^{-1} . For the electrical and thermoelectric (TE) measurements, all CZTS single crystals were cut along a - and c -axes, which the (200)/(004) reflect plane can be observed by XRD in Supplementary Fig. 1c.

Compositional properties

The compositional ratios (Cu:Zn:Sn:S) of each sample are 1.97:1.04:0.97:4.02 (**Sample 1**), 1.85:1.06:1.02:4.07 (**Sample 2**), 1.83:1.07:1.01:4.09 (**Sample 3**), and 1.87:1.05:1.03:4.05 (**Sample 4**) in Supplementary Table 1. In this study, our strategy for improvement of TE properties is the utilization of shallower Cu vacancy (V_{Cu}) acceptor by Cu-poor, Zn-rich condition than Cu on Zn antisite (Cu_{Zn}) for reported quaternary compounds by Cu-rich, Zn-poor condition. In addition, the concentration of unintentional impurities detected by ICP-AES is summarized in Supplementary Table 2, for which the effect of Na-doping is confirmed. The unintentional impurity concentrations are fairly low (less than several hundreds of ppb level).

Thermal conductivity for high temperature region

The thermal conductivity was calculated from $\kappa = \lambda C_p D$. The thermal diffusivity coefficient λ was measured along the same direction as the electrical and TE measurements using the laser flash diffusivity method. The specific heat capacity C_p was measured by differential scanning calorimetry (DSC). Both measurements were carried out in the range from 300-800 K.

ZT measurement uncertainty

The measurement of conductivity σ , Seebeck coefficient S , and thermal conductivity κ (calculated from λ , C_p , and D), each has an uncertainty of 2 % to 12 %. The uncertainty in ZT can be expressed as Eq. (s4) by each measurement uncertainties.

$$\frac{\Delta ZT}{ZT} = \frac{\Delta \sigma}{\sigma} + 2 \frac{\Delta S}{S} + \frac{\Delta \lambda}{\lambda} + \frac{\Delta C_p}{C_p} + \frac{\Delta D}{D} \quad (\text{s4})$$

The multiple measurements for all properties were carried out, and then we found good repeatability. The uncertainty of σ is 4-8% (Supplementary Fig. 2a) and S is 2-6% (Supplementary Fig. 2b), and the measurement uncertainty of the power factor PF is 8-20% (Supplementary Fig. 2c) by combining the uncertainties of σ and S . The uncertainty of κ is 8-12% (Supplementary Fig. 3a) comprising those of 3-5% for λ (Supplementary Fig. 3b), 3-5% for C_p (Supplementary Fig. 3c), and 2% for D . The combined uncertainty for all measurements involved in the calculation of ZT is within 30 % in Supplementary Fig. 4. The ZT for **sample 3** (Na: 0.1 mol% doped) ranges 1.4 to 1.9 at 800 K.

Temperature dependence of mobility

The measured hole mobility data as a function of temperature for each sample in Supplementary Fig. 5. Firstly, we discuss two distinct regions roughly: the phonon scattering for high temperature ($T > 300$ K) and the ionized impurity scattering for low temperatures ($T < 100$ K) with a transition in between. The lines included in Supplementary Fig. 5a are the fitting to $\mu \sim$

T^k . The k values for low temperatures indicates more than 1.5, which suggests a hopping conduction by intrinsic point defects. The slope in the higher temperature region follows a T^{-k} behavior of a semiconductor, which means that typical lattice scattering by the acoustic phonon is dominant. The absolute k values for high temperature are higher with off-stoichiometry and Na-doping and these coincide with lower thermal conductivity.

For modeling the scattering processes of kesterite compounds, we have considered some scattering terms that is impurity, lattice, polar optical and neutral impurity scatterings from various reported results. In this study, we attempt to fit data by impurity conduction and lattice scattering processes. Because only the hopping conduction between localized states in the impurity band is dominant for the low temperature region $T < 100$ K in our previous studies [S4-5], it is not described as typical $\sim T^k$ relation. The impurity mobility μ_i in this study are expressed as exponential function (s1) based on hopping conduction [S6]

$$\mu_i = \frac{H}{k_b T} \exp\left(-\frac{W}{k_b T}\right) \quad (\text{s1})$$

where H is a constant, W the hopping activation energy and k_b is Boltzmann constant. The total lattice mobility in CZTS is consisted of acoustic (AC) and non-polar (NPO) phonon scattering due to localized short-range non-cubic lattice distortions and non-parabolic valence band caused from the deformation of optical lattice, which is more dominant than polar optical scattering in p-type conduction at high temperature [S7]. This combined AC and NPO model mobility is well considered as equation (s2) [S7].

$$\mu_{AC, NPO} = 3.17 \times 10^{-5} \frac{\rho u^2 S(\theta, \eta, T)}{(m_{v1}/m_e)^{5/2} E_{AC}^2} T^{-3/2} \quad (\text{s2})$$

$$u = \frac{k_B \theta_D}{\hbar} \left(\frac{V}{6\pi^2} \right)^{1/3}$$

$$S(\theta, \eta, T) = (1 + A\eta)^{-1}$$

$$A = \frac{1.34z}{e^z - 0.914}$$

$$\eta = (E_{\text{NPO}}/E_{\text{AC}})^2$$

where ρ is the density, u is the average velocity of sound, m_{v1}/m_e is the hole effective mass ratio of topmost valence band, θ_D is the Debye temperature, V is the average atomic volume, E_{AC} and E_{NPO} are the deformation potentials for the acoustic and optical phonons respectively, θ is the characteristic temperature of the optical phonons and $z = \theta/T$. The values of ρ , u , θ_D and V are determined from our experimental measurements. The density of state (DOS) mas of the valence band is determined by calculation ellipsoidal expression $m_{v1} = (m_{v1}^{\perp} m_{v1}^{\perp} m_{v1}^{\parallel})^{1/3}$. All parameters on scattering process are shown in Supplementary Table 4. The total holr mobility μ of CZTS are calculated by using Mathiessen's approximation from Eqs. (s1)-(s2).

$$\frac{1}{\mu} \approx \frac{1}{\mu_I} + \frac{1}{\mu_{\text{AC,NPO}}} \quad (\text{s3})$$

In Supplementary Figs 5b-d the hole mobility fitted data for CZTS samples in this study are plotted by using Eq. (s3). Excellent quantitative agreements between the calculation and the experimental values over the whole temperature range have obtained for all samples. Considering high temperature region > 500 K for TE material, the lattice scattering combined with AC and NPO is most important mechanism accounting for 60-70% of total mobility. On the other hand, impurity conduction accounts for 30-40% of total mobility. Despite the increase in hole concentration, the hole mobility can be improved by off-stoichiometry and Na-doping which is because of shallower thermal energy W by screening effect [S5].

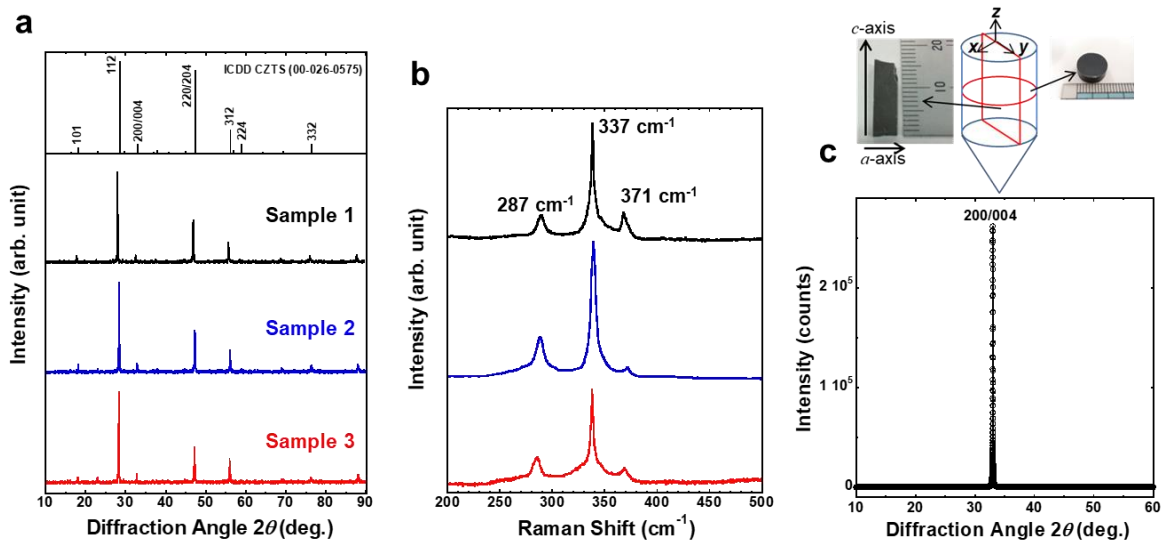
Stability for high temperature

Thermogravimetric analysis (TGA) was performed on Rigaku Thermo plys EVO2/TG-DTA under a N_2 flow in the temperature range from 300-800 K with a rate of 5 K/min in

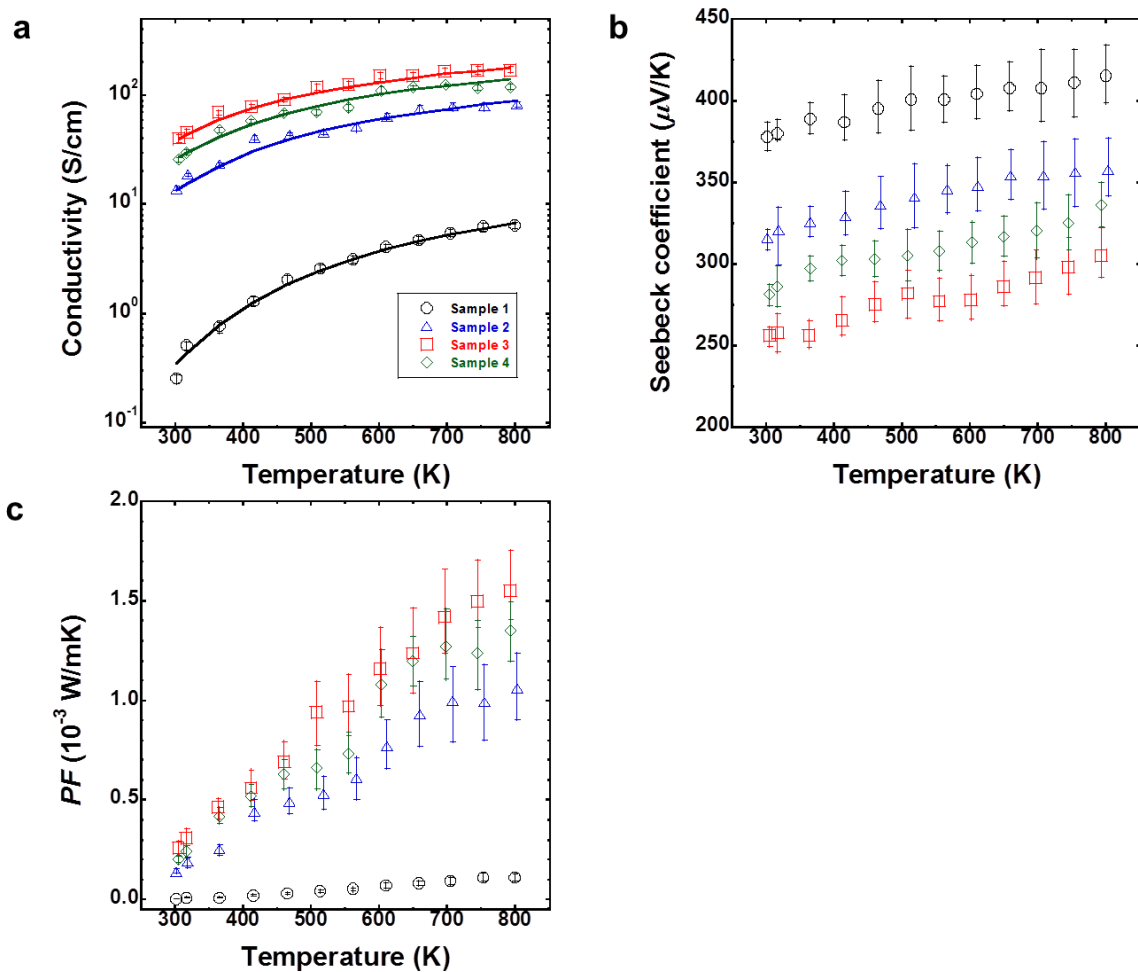
Supplementary Fig. 6. The TGA results indicate that all samples are stable at the temperature up to 800 K in N₂ atmosphere.

Electronic band structure of Na-doped CZTS

We employ a 2×2×1 supercell containing 64 atom sites which is constructed by extending the optimized unit cell for Na-doping related complex in CZTS. The Na atom substituting on Cu 2a site (Na_{Cu} defect) is lowest formation energy where is 6.25% Na doping concentration. Supplementary Figs. 7-8 show the calculated electronic band structures and the calculated density of states (DOS) for the non- and Na-doped CZTS by using density of functional theory (DFT). The increased DOS by Cu-deficit and Na-doping could be observed from experimental measurement in this study. However, there is no significant Na effect on electronic band structure and DOS in the vicinity of Γ point. The hole effective mass is slightly increased by Na-doping in Supplementary Table 6. Other possible Na effect on DOS is the increasing of Na-related substitution acceptor defect such as Na substituting on Zn site (Na_{Zn}) with low formation energy or defect complex.

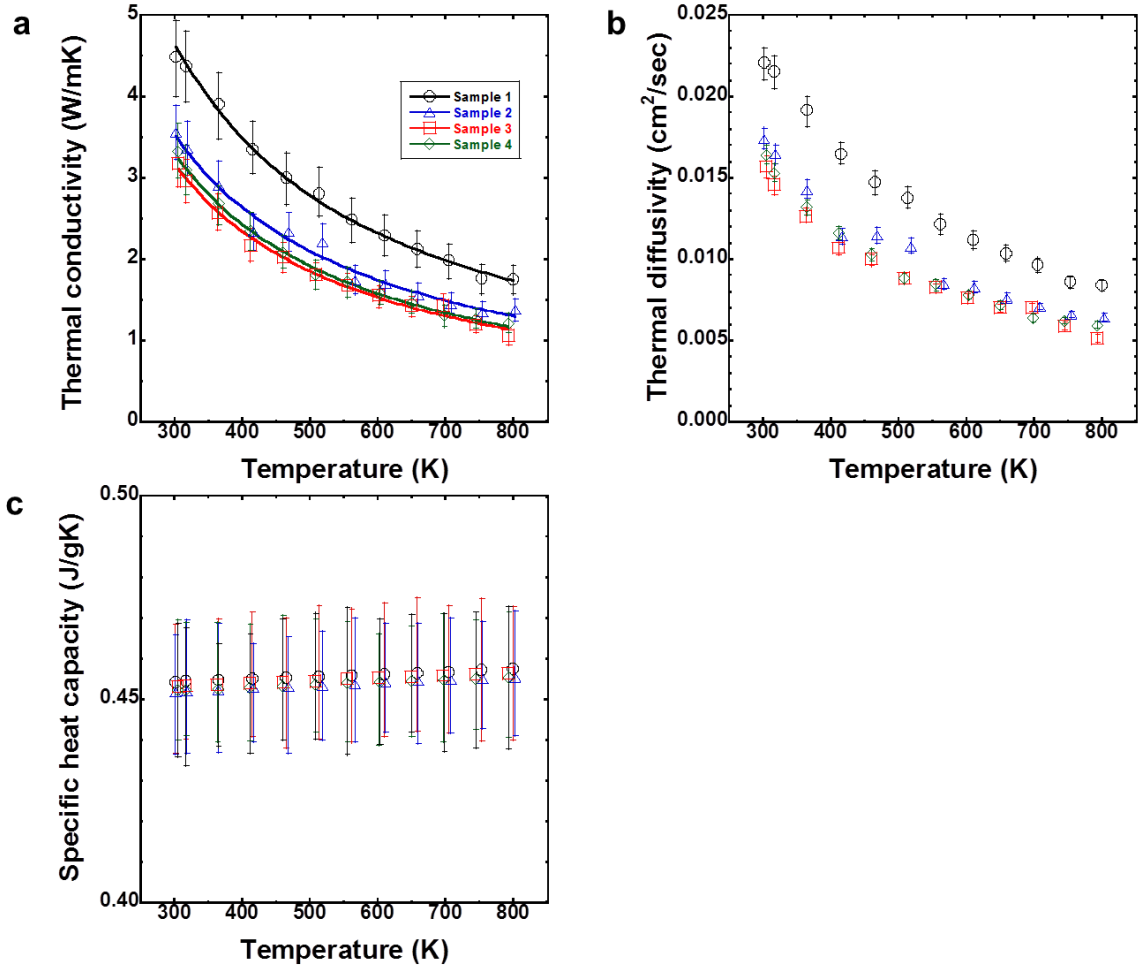


Supplementary Fig. 1 Structural properties for samples 1 (stoichiometric), 2 (Cu-poor), and 3 (Na: 0.1 mol%) for confirming of kesterite phase. **a**, the powder XRD patterns; **(b)** Raman spectroscopy; **(c)** XRD of the cutting plane along *a*- and *c*-axes. Inset images: how crystals were cut for directional measurements.

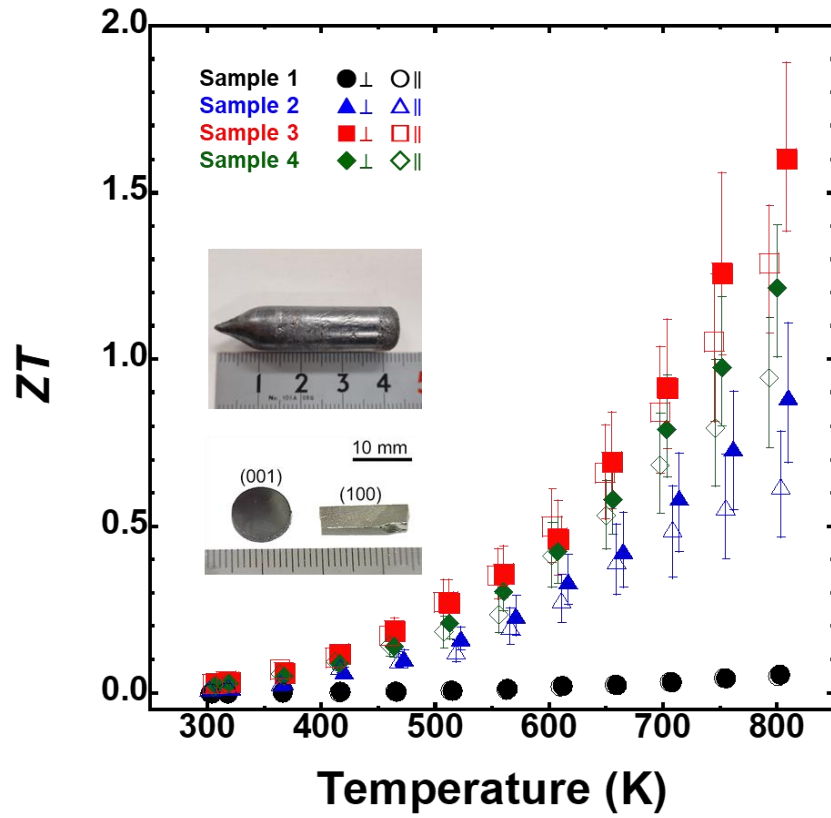


Supplementary Fig. 2 The reproducibility of TE characterization for CZTS single crystals.

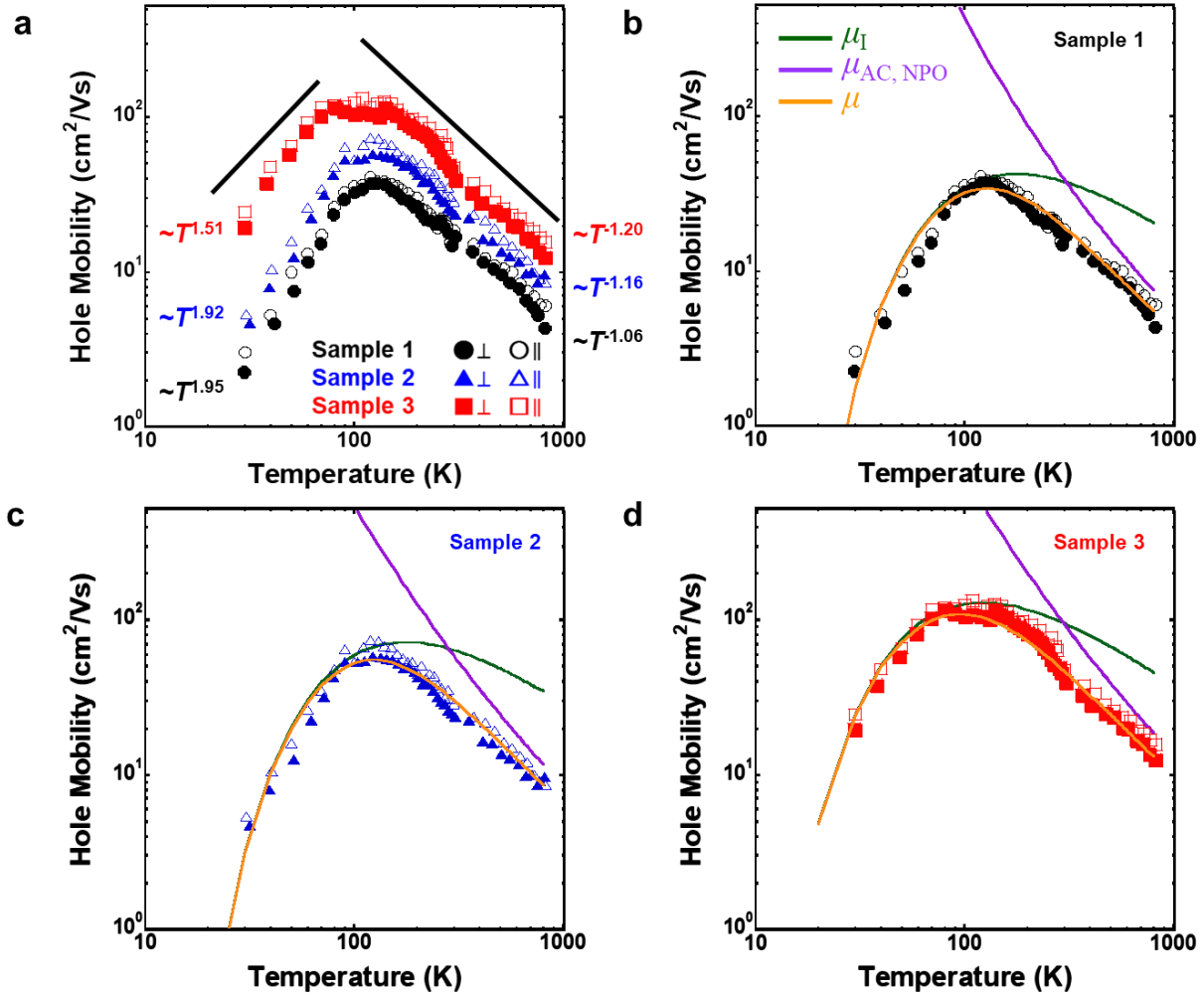
Temperature dependence of **a**, electrical conductivity σ ; **b**, Seebeck coefficient S ; **c**, power factor PF by multiple measurements. The uncertainty of σ is 4-8 % and S is 2-6 %, and the measurement uncertainty of PF is 8-20 %.



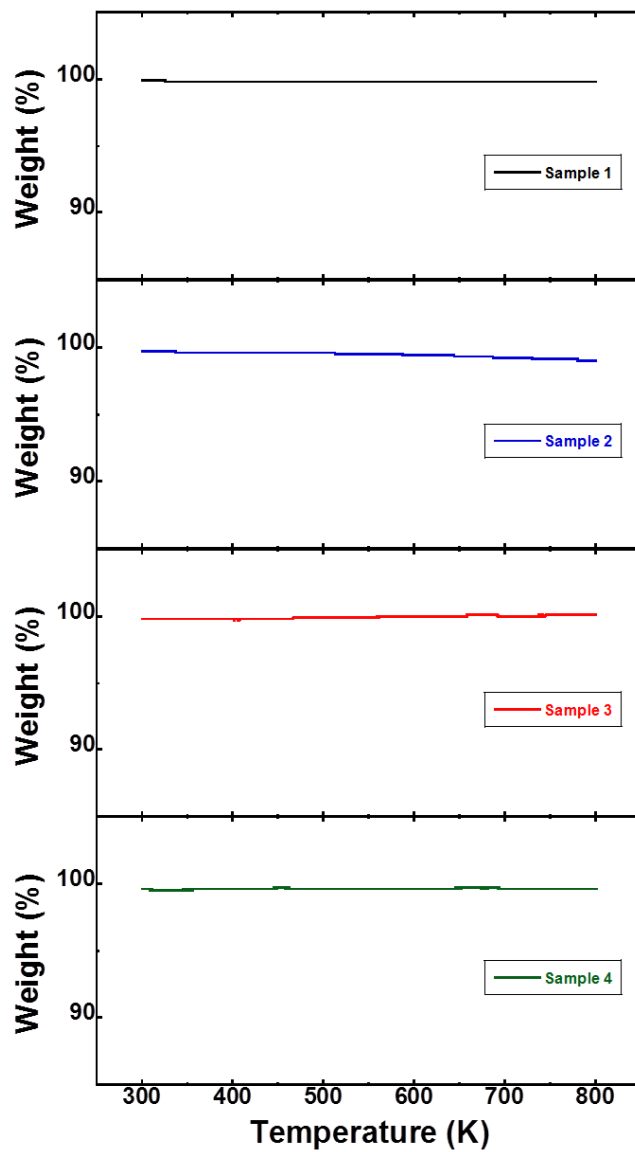
Supplementary Fig. 3 The reproducibility of thermal transport properties for CZTS single crystals. Temperature dependence of **a**, thermal conductivity $\kappa = \lambda C_p D$; **b**, thermal diffusivity λ ; **c**, specific heat capacity C_p by multiple measurements. The density D between 4.4-4.5 g/cm^3 were measured using the Archimedes method at room temperature. The uncertainty of κ is 8-12 % comprising those of 3-5 % for λ , 3-5 % for C_p , and 2 % for D .



Supplementary Fig. 4 The reproducibility of the dimensionless figure of merit ZT for CZTS single crystals. The ZT measurement uncertainty is about 30 %.

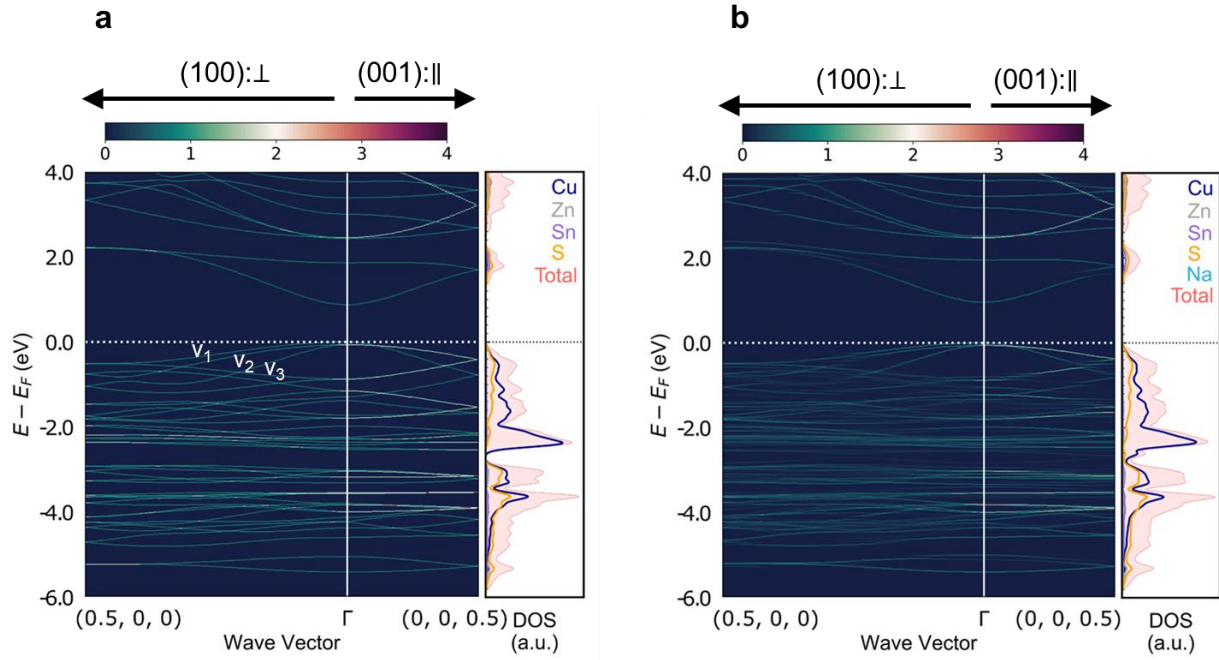


Supplementary Fig. 5 Temperature dependence of the measured hole mobility in CZTS single crystals. a, Fitting by T^k relation; **b-d,** Fitting by the combination of hopping conduction μ_I and acoustic (AC) and non-polar (NPO) phonon scattering $\mu_{AC, NPO}$. The slope parameter k at low temperature $T < 100$ K are higher than 1.5, which indicates hopping conduction in the impurity band. The absolute k values at high temperature $T > 300$ K are less than 1.5 expected for typical lattice scattering. Total hole mobility μ composed of μ_I and $\mu_{AC, NPO}$ is excellent agreement with experimental data.

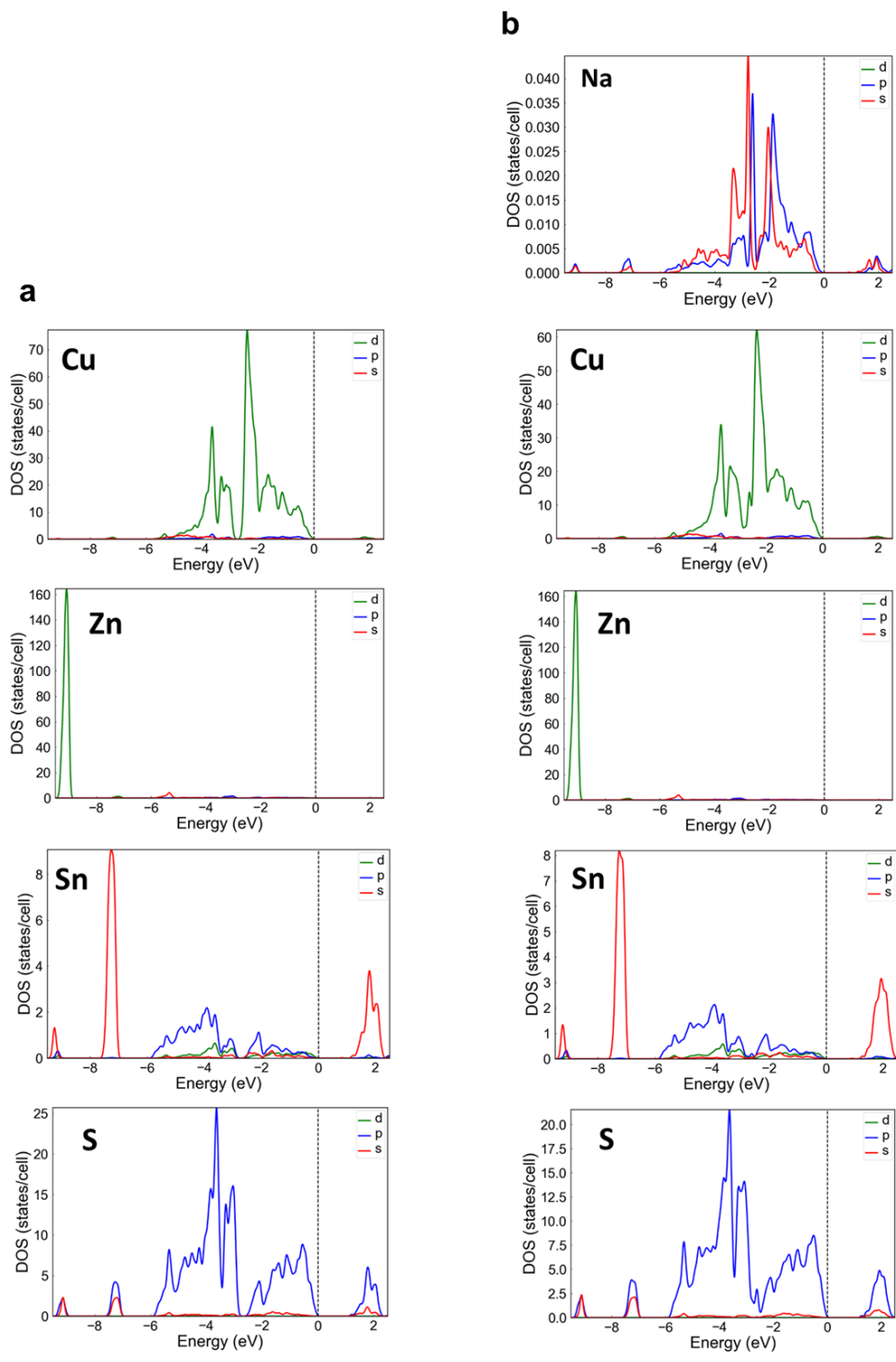


Supplementary Fig. 6 The thermogravimetric analysis (TGA) measurements of samples 1-4.

All samples are stable at the temperature up to 800 K in N₂ atmosphere.



Supplementary Fig. 7 Electronic band structures along the two symmetry directions (100) and (001) by DFT calculation. a, Non-doped; b, 6.25% Na-doped CZTS by DFT calculation. The top of the valence band is split into the topmost (v_1) and second (v_2) bands with Γ_{7+8} symmetry and the third band (v_3) with Γ_{5+6} symmetry. Dashed line denote the Fermi energy. The color scale represents the number of band crossing.



Supplementary Fig. 8 Calculated DOS of each atoms. **a**, Non-doped; **b**, 6.25% Na-doped CZTS. Dashed line denote the Fermi energy.

Supplementary Table 1 The detailed composition of each sample determined by ICP-AES.

	Cu (at.%)	Zn (at.%)	Sn (at.%)	S (at.%)
Sample 1	24.8	12.8	12.3	50.1
Sample 2	23.8	13.3	12.0	50.9
Sample 3	24.2	13.3	12.2	50.3
Sample 4	24.0	13.1	12.3	50.6

Supplementary Table 2 Unintentional impurity levels detected by ICP-AES in the CZTS single crystals.

Impurity (ppb)	Sample 1	Sample 2	Sample 3	Sample 4
C	430	530	310	320
N	30	25	15	35
O	320	390	270	230
Mg	650	550	450	600
Al	320	180	150	210
Si	230	450	350	320
Ni	60	55	40	50
Fe	45	35	30	20

Supplementary Table 3 Results and parameters of the CZTS single crystals determined as described in the main text.

	Electrical properties at 300 K			Conduction parameters		AS measurement			
	p (cm^{-3})	σ (S/cm)	μ (cm^2/Vs)	σ_B (S/cm)	E_A (meV)	$E(\omega_0)$ (meV)	Integrated N_t (cm^{-3})	V_{bi} (V)	W_d (nm)
Sample 1	3.2×10^{16}	0.13	25.1	41	125	100	1.2×10^{16}	0.72	252
Sample 2	8.1×10^{17}	6.0	45.4	278	79	80	3.5×10^{17}	0.64	220
Sample 3	3.0×10^{18}	42.8	89.3	455	64	65	2.2×10^{18}	0.61	198
Sample 4	1.8×10^{18}	26.9	76.9	400	71	73	9.2×10^{17}	0.63	205

Supplementary Table 4 Scattring parameters of the CZTS single crystals determined from temperature dependence of hole mobility.

	H (eVcm^2/Vs)	W (meV)	E_{AC} (eV)	E_{NPO} (eV)	D (g/cm^3)	u (cm/s)	m_{v1}/m_e	θ_D (K)	θ (K)
Sample 1	1.8	15.3	10.0	15.0					
Sample 2	3.0	12.4	10.0	13.0	4.405	2.84×10^5	0.47	302	310
Sample 3	3.7	10.5	8.0	12.0					

Supplementary Table 5 High temperature TE properties of CZTS single crystal compared to some relating quaternary materials.

Material	σ (S/cm)	S (μ V/K)	PF (10^{-3} W/mK ²)	κ (W/mK)	ZT	T_{ZT} (K)	Ref.
Sample 3	165	347	1.86	0.95	1.6	800	This work
Cu _{2.19} Zn _{0.8} Sn _{0.75} S _{3.53}	13.9	301	0.125	0.645	0.14	700	S8
Cu ₂ ZnSn _{0.9} In _{0.1} Se ₄	102	300	0.92	0.82	0.95	850	S9
Cu _{2.2} Zn _{0.8} SnSe ₄	157	192	0.58	0.54	0.86	800	S10
Cu _{2.15} Cd _{0.85} SnSe _{3.9}	67	180	0.22	0.21	0.71	685	S11
Cu ₂ CoSnSe ₄	130	230	0.69	0.84	0.7	850	S12
Cu _{2.15} Zn _{0.85} GeSe _{3.9}	206	120	0.30	0.4	0.55	723	S13
Cu ₂ MnSnSe ₄	52	270	0.37	0.6	0.52	850	S12
Cu ₂ Zn _{0.4} Fe _{0.6} SnSe ₄	75	232	0.40	0.7	0.46	800	S14
Cu ₂ FeSnSe ₄	64	235	0.35	0.75	0.4	850	S12

Supplementary Table 6 Anisotropy of the effective hole masses (m_n for $n = v_1, v_2,$ and v_3 in Fig. 1) in CZTS. m_e is electron mass.

The transverse \perp masses are determined from the energy dispersions in (100) direction, and the longitudinal \parallel masses are determined from the dispersions in (001) direction.

	$m_{v_1}^{\perp}[m_e]$	$m_{v_1}^{\parallel}[m_e]$	$m_{v_2}^{\perp}[m_e]$	$m_{v_2}^{\parallel}[m_e]$	$m_{v_3}^{\perp}[m_e]$	$m_{v_3}^{\parallel}[m_e]$
Non-doped	0.77	0.17	0.78	0.76	0.16	0.76
Na-doped	0.81	0.17	0.84	0.79	0.17	0.79

Supplementary Reference

- S1. I. D. Olekseyuk, I. V. Dudchak and L. V. Piskach, *J. Alloy. Compd.*, 2004, **368**, 135-143.
- S2. A. Nagaoka, K. Yoshino, H. Taniguchi, T. Taniyama and H. Miyake, *J. Crystal Growth*, 2012, **341**, 38-41.
- S3. A. Nagaoka, M. A. Scarpulla and K. Yoshino, *J. Crystal Growth*, 2016, **453**, 119-123.
- S4. A. Nagaoka, H. Miyake, T. Taniyama, K. Kakimoto, and K. Yoshino, *Appl. Phys. Lett.* 2013, **103**, 112107.
- S5. A. Nagaoka, H. Miyake, T. Taniyama, K. Kakimoto, Y. Nose, M. A. Scarpulla, and K. Yoshino, *Appl. Phys. Lett.* 2014, **104**, 152101.
- S6. M. Cutler and N. F. Mott, *Phys. Rev.* 1969, **181**, 1336.
- S7. J. D. Wiley, and M. DiDomenico, Jr, *Phys. Rev. B* 1070, **2**, 427.
- S8. H. Yang, L. A. Jauregui, G. Zhang, Y. P. Chen and Y. Wu, *Nano Lett.*, 2012, **12**, 540-545.
- S9. X. Y. Shi, F. Q. Huang, M. L. Liu and L. D. Chen, *Appl. Phys. Lett.*, 2009, **94**, 122103.
- S10. Y. Dong, H. Wang and G. S. Nolas, *Phys. Status Solidi RRL*, 2014, **8**, 61-64.
- S11. M. Ibáñez, D. Cadavid, R. Zamani, N. G. -Castelló, V. I. -Roca, W. Li, A. Fairbrother, J. D. Prades, A. Shavel, J. Arbiol, A. P. -Rodríguez, J. R. Morante and A. Cabot, *Chem. Mater.*, 2012, **24**, 562-570.
- S12. Q. Song, P. Qiu, F. Hao, K. Zhao, T. Zhang, D. Ren, X. Shi and L. Chen, *Adv. Electron. Mater.*, 2016, **2**, 1600312.
- S13. M. Ibáñez, R. Zamani, A. LaLonde, D. Cadavid, W. Lin, A. Shavel, J. Arbiol, J. R. Morante, S. Gorsse, G. J. Snyder and A. Cabot, *J. Am. Chem. Soc.*, 2012, **134**, 4060-4063.
- S14. Y. Dong, H. Wang and G. S. Nolas, *Inorg. Chem.*, 2013, **52**, 14364-14367.